J. Fluid Mech. (1976), *vol.* 73, *part* 2, *pp.* 333–351
Printed in Great Britain

Internal electrohydrodynamic instability and mixing of fluids with orthogonal field and conductivity gradients

By JAMES F. HOBURG AND JAMES R. MELCHER
Massachusetts Institute of Technology, Cambridge

(Received 8 April 1975 and in revised form 30 August 1975)

The interface between two miscible fluids which have identical mechanical properties but disparate electrical conductivities and are stressed by an equilibrium tangential electric field is studied experimentally and theoretically. A bulk-coupled electrohydrodynamic instability associated with the diffusive distribution of fluid conductivity at the interface is experimentally observed.

The configuration is modelled using a layer of exponentially varying conductivity spliced on each surface to a constant-conductivity fluid half-space. Overstable (propagating) modes are discovered and characterized in terms of the complex growth rate and fastest growing wavenumber, with the conductivity ratio and an inertia–viscosity time-constant ratio as parameters. In the low inertia limit, growth rates are governed by the electric–viscous time $\tau = \eta/\epsilon E^2$. Instability is found also with the layer of varying conductivity bounded by rigid equipotential walls. A physical mechanism leading to theoretically determined fluid streamlines in the form of propagating cells is described.

At relatively high electric fields, large-scale mixing of the fluid components is observed. Photocell measurements of distributions of average fluid properties demonstrate evolution in time on a scale determined by τ.

1. Experimental motivation

Experimental studies involving the application of an electric field tangential to the interface between two miscible fluids of identical mechanical properties but disparate electrical conductivities lead to unexpected phenomena. Figure 1 shows a drawing of an electrohydrodynamic flow cell. Microscope slides allow optical projection through the cell from a tungsten-arc point light source. Two fluids enter via inlet tubes at the top and bottom respectively. Removal via the outlet tubes at the sides allows formation of a clean horizontal interface midway up the cell. An electric field is applied tangential to the interface by means of wire electrodes running vertically along the sides.

The liquid used is Mazola corn oil. Pure corn oil enters through the bottom inlet tube. That entering at the top inlet tube is doped in electrical conductivity with anti-static fluid and dyed with red dye. Depending upon the experiment to be performed, the upper fluid is used straight (as doped and dyed) or diluted with pure corn oil to $\frac{1}{20}$ concentration by volume. The various physical properties are listed in table 1.

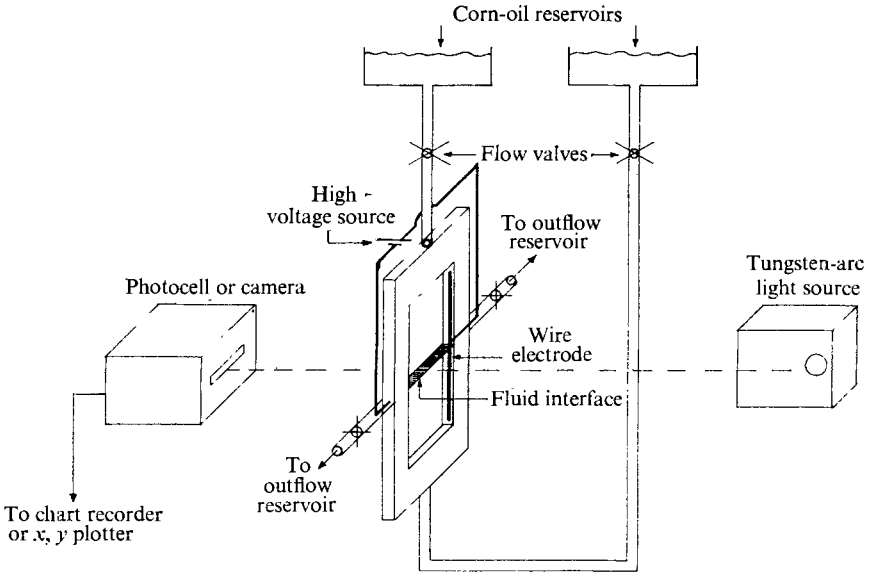

FIGURE 1. Experimental flow cell and optical configuration. A horizontal interface between fluid components is formed midway up the cell. Wire electrodes impose a tangential electric field.

Density	$\rho = 0{\cdot}992 \times 10^3$ kg/m^3
Viscosity	$\eta = 6 \times 10^{-2}$ kg/m s
Permittivity	$\epsilon = 3{\cdot}1\ \epsilon_0 = 2{\cdot}74 \times 10^{-11}$ farad/m
Conductivity	
Pure	$\sigma = 4{\cdot}05 \times 10^{-11}$ mho/m
$\frac{1}{20}$ mixture	$\sigma = 1{\cdot}05 \times 10^{-9}$ mho/m
Straight doped and dyed	$\sigma = 8{\cdot}1 \times 10^{-9}$ mho/m

TABLE 1. Corn-oil properties

Samples of still photographs obtained by projecting the image of the cell directly onto the shutter of a 35 mm camera are shown in figure 2 (plate 1). The lower, clear fluid is pure corn oil, while the upper, dark fluid is the $\frac{1}{20}$ mixture of doped and red-dyed corn oil. The conductivity ratio in this case is $R = 25{\cdot}9$. For each of the three sequences shown, a clean interface is formed, then allowed to diffuse for a known time before application of the field. In the first two sequences ($E = 2{\cdot}42 \times 10^4$ V/m and $E = 1{\cdot}21 \times 10^4$ V/m respectively) the interface has diffused for 1 h, while in the last sequence ($E = 1{\cdot}82 \times 10^4$ V/m) it has diffused for 4 h. Thus the last sequence begins with an interface structure twice as broad as the first two. Photographs were taken at the indicated times after the instant the electrical source was switched on.

In each sequence, note the appearance, on the scale of the interface structure, of slanted fronts, originating at the outer edges and propagating towards the

centre. The distance between fronts in the last sequence is double the distance between fronts for the first two. The slant angles of fronts vary between photographs, but lie in the range 20°–30°.

The respective time intervals between photographs are scaled to $1/E^2$. Note that, with this scaling, the sequence of events appears to be quite similar for the two sequences with identically diffuse initial interfaces. In real time, the second sequence evolves over a period four times as long as the first.

The theory to follow is aimed at a basic understanding of the phenomenon observed in figure 2: an electrohydrodynamic instability on the scale of the structure of the interface between fluid components of differing conductivities experiencing a tangential electric field.

2. High field mixing

The photographs shown in figure 2 all correspond to relatively low values of the electric field. For higher values ($E \sim 10^5$ V/m and higher), the interface curves, buckles and folds over on itself. In static equilibrium, there is no electrical force density. The rotational character of the electric force density created by the instability is evident as fluid components roll and swirl into one another.

Figure 3 (plate 1) demonstrates the sort of mixing attainable in relatively short times at relatively high values of the electric field. The fluid orientation has been reversed here, with the pure corn oil on top. Straight dyed and doped corn oil is used in the lower part of the cell, yielding a conductivity ratio of $R = 200$. Motions of the kind shown here are of obvious interest with regard to practical mixing operations (Uhl & Gray 1966). An important consideration in the large-scale processes shown is viscous drag due to the proximity of the front and back cell walls.

No simple theory can account for the complex and nonlinear processes observed at these high field values. However it is possible to determine scaling laws for average mixture properties as functions of position.

A quantitative description of the mixing process exemplified by figure 3 is accomplished with the use of a photocell, providing an electrical signal with magnitude directly proportional to the intensity of light incident on a narrow slit. The photocell is positioned behind the mixing cell, so that the intensity of light from the tungsten-arc source depends upon the optical properties of fluid at a given level in the cell.

The vertical positioning is such that light incident on the photocell slit has passed through the experimental cell just above the interface. As dark fluid is swept up into the region above the initial interface, the light intensity incident on the photocell slit is diminished, and a chart recorder sensing photocell output provides a time history of the mixing process at one vertical position in the cell. (Variations in the horizontal direction are automatically averaged out by this method.)

Figure 4 shows plots of light intensity as a function of time for six different values of the electric field. The time scale here is normalized using the electric-

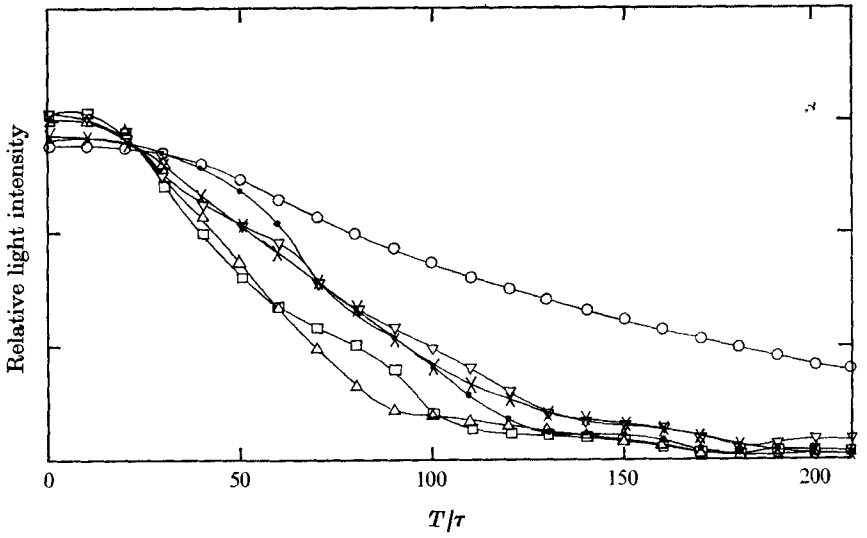

FIGURE 4. Relative light intensity through experimental cell *vs.* time for various values of electric field. Time scale is normalized to $\tau = \eta/\epsilon E^2$. High-field mixing processes scale in time with τ, provided inertia is negligible. •—•, $0{\cdot}606 \times 10^5$ V/m; ▽—▽, $1{\cdot}21 \times 10^5$ V/m; □—□, $1{\cdot}92 \times 10^5$ V/m; △—△, $2{\cdot}42 \times 10^5$ V/m; ×—×, $3{\cdot}84 \times 10^5$ V/m; ○—○, $6{\cdot}06 \times 10^5$ V/m.

viscous time $\tau = \eta/\epsilon E^2$. This time will assume prime importance in the theory to follow. It is evident that the mixing process evolves on the scale of the cell over times of order $10^2\tau$. The point here is that, except for the highest value of the electric field, the various normalized curves are reasonably close to one another, even though the run at $0{\cdot}606 \times 10^5$ V/m evolved in real time over a period 40 times as long as the run at $3{\cdot}84 \times 10^5$ V/m. The scaling of the mixing process with τ is thus experimentally confirmed. At the highest field value ($E = 6{\cdot}06 \times 10^5$ V/m) inertia apparently plays a role in the electrohydrodynamic process, with growth occurring less rapidly than would be predicted on the basis of a purely viscous flow.

Further quantitative data are obtained in a second photocell experiment, this time allowing a determination of the fluid distribution over the vertical length of the cell. The vertical position of the photocell slit may be varied over a range of 2 cm on either side of the initial fluid interface. An electrical signal corresponding to the cell position drives one scale of an x, y plotter, with the light-intensity signal driving the second scale. Thus, by running the photocell over the mixing cell's length, a curve describing the fluid-component distribution is obtained. The $\frac{1}{20}$ mixture is used for the dark fluid because, for dilutions of $\frac{1}{20}$ and less, the light intensity through the cell is directly proportional to the percentage of clear corn oil in the mixture.

Because the flows involved are viscosity dominated, it is possible to apply an electric field for a given time, switch off the field, take a photocell distribution run, and switch the field back on to continue the experiment. (Lengths small

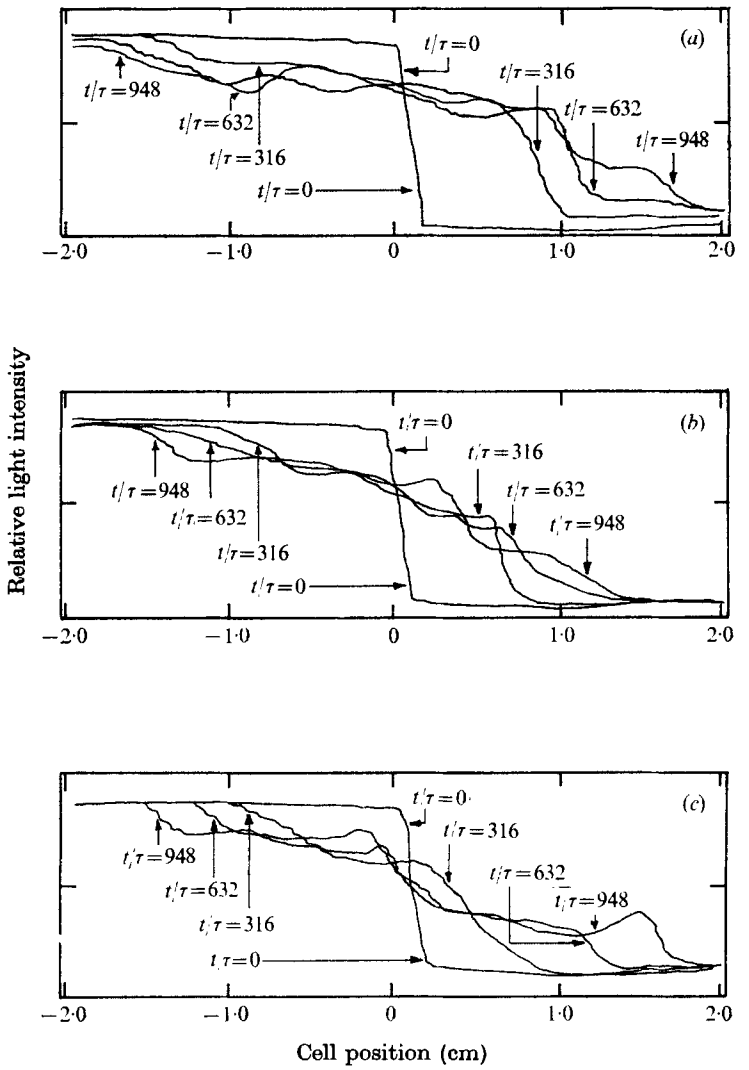

FIGURE 5. Relative light intensity through experimental cell *vs.* cell position for various times. Times are normalized to $\tau = \eta/\epsilon E^2$. Similarity of evolution for different values of electric field again confirms scaling with τ. (*a*) $E = 0{\cdot}606 \times 10^5$ V/m. (*b*) $E = 1{\cdot}82 \times 10^5$ V/m. (*c*) $E = 6{\cdot}06 \times 10^5$ V/m.

enough for diffusional processes to alter the distribution during the time the field is off are of no concern here.) The fineness with which the distribution may be determined is limited by the photocell slit width (1·6 mm).

Figure 5 shows the evolution of fluid-component distributions for values of the electric field varying by a factor of 10. In each case, distributions are determined at three times in addition to the initial clean interface distribution. The times at which plots are made are chosen such that t/τ takes on the same three values in each case. Thus the run with the lowest field spans a time period 100 times as long as that with the highest field.

Again, strong experimental evidence of scaling of the mixing process with τ is provided by the similarities of the evolution for various values of the electric field. At the highest field value, some details of the plots have a somewhat altered character, possibly the result of inertial effects beginning to have a noticeable influence on the motions.

3. Surface-coupled model

Surface-coupled phenomena, i.e. those which may be described in terms of interfacial motions, driven by an electric surface force density and resulting in time and space evolution of its position, magnitude, and direction, account for a wide variety of interactions involving electric fields in multiproperty systems. Accumulation of surface charge at interface saliencies often leads to a surface force which tends to cause growth of perturbation displacements from a static equilibrium (Melcher 1972). Such instability, in its nonlinear stages, leads to mixing of fluid components initially separated by a flat interface.

It is natural to think of the experiment described in terms of a surface-coupled model. An interface between two fluid layers of differing conductivities σ_a and σ_b, but identical mechanical properties experiences a uniform equilibrium electric field E_0, initially tangential to the interface.

This problem is a special case of one considered by Melcher & Schwarz (1968). With all fluid properties continuous across the interface except conductivity, equation (34) of that paper reduces to two roots:

$$s = 0 \quad \text{or} \quad s = -\nu k^2. \tag{1}$$

In this limit, there is no electromechanical coupling at the interface, and these roots represent viscous decay only. The root $s = 0$ occurs because there is no restoring force in the face of perturbation interface displacements. The point to be emphasized here is the lack of coupling, and hence the lack of instability predicted by a linear surface-coupled model. Any instability based on a conductivity-jump model must arise from nonlinear coupling terms.

4. A bulk-coupled layer of varying conductivity: general equations

A surface-coupled model, linearized or not, clearly cannot account for effects occurring on the scale of the thickness of the interface itself. Figure 2 shows a process which occurs on a scale comparable to that which describes the diffusive distribution of conductivity at the junction between fluid layers. In the theory to follow, the aim is to relax the restriction that the region over which conductivity variation occurs be thin compared with lengths describing instability dynamics. The interaction, then, is bulk-coupled, with fluid properties modelled as varying in a continuous manner and fluid motions as driven by the volume force density, caused by fluid deformations.

Situations involving a junction between two miscible fluids of differing conductivities will, in general, involve diffusion as an ion transport mechanism, and hence as a governing mechanism in setting up the conductivity distribution.

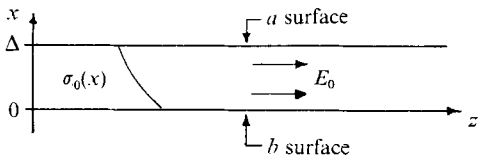

FIGURE 6. Varying-conductivity fluid layer experiencing uniform equilibrium tangential field $E_0\,\mathbf{i}_z$.

It is not meaningful to consider questions of electrohydrodynamic stability by assuming perturbations from an equilibrium state if, owing to diffusion, the equilibrium is evolving at a rate comparable to that of the perturbation dynamics. If, however, diffusion times are long compared with times describing instability dynamics, we may describe the junction by an equilibrium conductivity distribution, itself evolving slowly with time, and subject to electrohydrodynamic instability as modelled in a situation of static equilibrium. This is now assumed.

A layer of fluid, with equilibrium conductivity distribution $\sigma_0(x)$, extends from $x = 0$ to $x = \Delta$ and experiences a uniform equilibrium tangential electric field $E_0\,\mathbf{i}_z$ as shown in figure 6.

In the face of fluid motions, the conductivity distribution is altered, with diffusion always acting to smooth the distribution at any one instant. The same basic assumption regarding the relative size of time scales for perturbation dynamics and diffusion times leads to a model in which each elemental volume of fluid of fixed identity retains a constant conductivity $\sigma(x, y, z, t)$ as it moves with the fluid velocity $\mathbf{v}$:

$$\partial\sigma/\partial t + \mathbf{v}.\,\nabla\sigma = 0. \tag{2}$$

Said another way, in terms of an effective conductivity diffusion coefficient κ_{eff} and a characteristic dynamic length l and velocity U, it is asumed that the Péclet number $Ul/\kappa_{\text{eff}} \gg 1$ (Levich 1962).

Accumulation of a free charge density ρ_f in regions of conductivity variation is described by the equation of conservation of charge and Gauss' Law:

$$\nabla.\,[\sigma\mathbf{E} + \rho_f\mathbf{v}] + \partial\rho_f/\partial t = 0, \tag{3}$$

$$\nabla.\,\epsilon\mathbf{E} = \rho_f, \tag{4}$$

where $\mathbf{E}$ is the electric field intensity and ϵ the fluid permittivity. Charge relaxation in the pure corn oil occurs on a time scale $\epsilon/\sigma = 0{\cdot}68$ s. Of most concern here are fluid motions on time scales long compared with ϵ/σ, and hence instantaneous charge relaxation is assumed. That is, in terms of the characteristic length l and velocity U, the electric Reynolds number $\epsilon U/\sigma l \ll 1$ (Woodson & Melcher 1968), and the term $\partial\rho_f/\partial t + \mathbf{v}.\,\nabla\rho_f$ is neglected in combining (3) and (4):

$$(\sigma/\epsilon)\rho_f + \mathbf{E}.\,\nabla\sigma = 0. \tag{5}$$

It has been assumed here that ϵ = constant and the fluid is incompressible:

$$\nabla.\,\mathbf{v} = 0. \tag{6}$$

Equation (6) is satisfied by expressing $\mathbf{v}$ in terms of a stream function ψ:

$$\mathbf{v} = -\nabla \times \mathbf{i}_y \psi(x, z, t). \tag{7}$$

Because the quasi-static electric field is curl free, it may be expressed in terms of an electric potential Φ:

$$\mathbf{E} = -\nabla \Phi. \tag{8}$$

Poisson's equation may be derived from (4) and (8):

$$\nabla^2 \Phi = -\rho_f/\epsilon. \tag{9}$$

Finally, the effect of the electric force density $\rho_f \mathbf{E}$ on fluid motions is expressed by the Navier–Stokes equation:

$$\rho[\partial \mathbf{v}/\partial t + \mathbf{v} \cdot \nabla \mathbf{v}] + \nabla p = \eta \nabla^2 \mathbf{v} + \rho_f \mathbf{E}. \tag{10}$$

In equilibrium, the fluid is static and charge free. Small amplitude perturbations with dependence e^{st-ikz} are governed by linearized versions of (2), (5), (9) and the curl of (10) in terms of perturbation complex amplitudes $\hat{\sigma}$, $\hat{\phi}$, $\hat{\rho}_f$ and $\hat{\psi}$ respectively:

$$s\hat{\sigma} - ik\hat{\psi}(D\sigma_0) = 0, \tag{11}$$

$$(\sigma_0/\epsilon)\,\hat{\rho}_f - ikE_0\hat{\sigma} - (D\hat{\phi})\,(D\sigma_0) = 0, \tag{12}$$

$$(D^2 - k^2)\,\hat{\phi} = -\hat{\rho}_f/\epsilon, \tag{13}$$

$$s\rho[D^2 - k^2]\,\hat{\psi} = \eta[D^2 - k^2]^2\,\hat{\psi} - E_0 D\hat{\rho}_f, \tag{14}$$

where $D \equiv d/dx$.

Eliminating $\hat{\sigma}$, $\hat{\rho}_f$ and $\hat{\psi}$ yields one homogeneous equation in $\hat{\phi}$:

$$[D^2 - k^2]\left[\left(D^2 - k^2 - s\frac{\rho}{\eta}\right)\left(\frac{\sigma_0}{D\sigma_0}[D^2 - k^2] + D\right) + \frac{k^2}{s}\frac{\epsilon E_0^2}{\eta} D\right]\hat{\phi} = 0. \tag{15}$$

As is characteristic of bulk-coupled models, (15) has space-varying coefficients. For a general equilibrium conductivity distribution $\sigma_0(x)$, a numerical integration procedure is required to determine a solution.

5. Exponential $\sigma_0(x)$

There is one non-trivial distribution for which (15) has constant coefficients, i.e.

$$\sigma_0(x) = \sigma_b(\sigma_a/\sigma_b)^{x/\Delta}. \tag{16}$$

Here σ_a and σ_b represent the known values of the conductivity at the upper and lower surfaces of the layer, respectively, and the variation has an exponential character across the layer. For this distribution, the factor involving $\sigma_0(x)$ in (15) takes on a value independent of x:

$$\sigma_0(x)/D\sigma_0(x) = -\Delta/\ln R, \tag{17}$$

where

$$R \equiv \sigma_b/\sigma_a. \tag{18}$$

Substitution of (17) into (15) and assumption of solutions of the form $e^{\gamma x}$ gives a sixth-order normalized equation in γ:

$$[\gamma'^2 - k'^2][(\gamma'^2 - k'^2 - s'T/\tau)\,(\gamma'^2 - \gamma' \ln R - k'^2) - k'^2 s'^{-1}\gamma' \ln R] = 0, \tag{19}$$

where

$$k' \equiv k\Delta, \quad \gamma' \equiv \gamma\Delta, \quad s' \equiv s\tau, \quad T \equiv \rho\Delta^2/\eta, \quad \tau \equiv \eta/\epsilon E_0^2.$$

Two of the six solutions $\gamma' = \gamma_1', \ldots, \gamma_6'$ to (19) are $\gamma' = \pm k'$. For any given wavenumber k', growth rate s', and parameters T/τ and R, it is straightforward to solve the remaining quartic.

With all relations in terms of normalized perturbation complex amplitudes,

$$\left.\begin{aligned} \hat{\phi}' &\equiv \hat{\phi}/E_0\Delta, \quad \hat{\mathbf{v}}' \equiv \hat{\mathbf{v}}\tau/\Delta, \quad \hat{\psi}' \equiv \hat{\psi}\tau/\Delta^2, \\ \hat{\mathbf{S}}' &\equiv \hat{\mathbf{S}}/\epsilon E_0^2, \quad \hat{p}' \equiv \hat{p}/\epsilon E_0^2, \quad \hat{\mathbf{J}}' \equiv \hat{\mathbf{J}}/\sigma_a E_0 \end{aligned}\right\} \tag{20}$$

(where $\mathbf{S}$ represents fluid stress), the potential distribution is expressed as a linear combination of solutions of the form $e^{\gamma x}$:

$$\hat{\phi}' = \sum_{n=1}^{6} \hat{\phi}_n' \exp(\gamma_n' x/\Delta). \tag{21}$$

The various electrical and mechanical perturbation complex amplitudes within the layer evaluated in matrix form at the a and b surfaces are

$$\mathbf{V} = \mathbf{H}\mathbf{A}, \quad \mathbf{S} = \mathbf{G}\mathbf{A}, \tag{22), (23}$$

where

$$\mathbf{V} \equiv \begin{bmatrix} \hat{v}_x'^a \\ \hat{v}_x'^b \\ \hat{v}_z'^a \\ \hat{v}_z'^b \\ \hat{\phi}'^a \\ \hat{\phi}'^b \end{bmatrix}, \quad \mathbf{S} \equiv \begin{bmatrix} \hat{S}_x'^a \\ \hat{S}_x'^b \\ \hat{S}_z'^a \\ \hat{S}_z'^b \\ \hat{J}_x'^a \\ \hat{J}_x'^b \end{bmatrix}, \quad \mathbf{A} \equiv \begin{bmatrix} \hat{\Phi}_1' \\ \hat{\Phi}_2' \\ \hat{\Phi}_3' \\ \hat{\Phi}_4' \\ \hat{\Phi}_5' \\ \hat{\Phi}_6' \end{bmatrix} \tag{24}$$

and $\mathbf{H}$ and $\mathbf{G}$ are 6×6 matrices, with entries defined by

$$H_{1n} = \frac{is'}{k' \ln R}[\gamma_n'^2 - \gamma_n' \ln R - k'^2] \exp \gamma_n', \tag{25a}$$

$$H_{2n} = \frac{is'}{k' \ln R}[\gamma_n'^2 - \gamma_n' \ln R - k'^2], \tag{25b}$$

$$H_{3n} = \frac{s'\gamma_n'}{k'^2 \ln R}[\gamma_n'^2 - \gamma_n' \ln R - k'^2] \exp \gamma_n', \tag{25c}$$

$$H_{4n} = \frac{s'\gamma_n'}{k'^2 \ln R}[\gamma_n'^2 - \gamma_n' \ln R - k'^2], \tag{25d}$$

$$H_{5n} = \exp \gamma_n', \quad H_{6n} = 1, \tag{25e, f}$$

$$G_{1n} = \frac{1}{k'}\left[-\frac{1}{\ln R}\frac{is'\gamma_n'}{k'^2}(\gamma_n'^2 - \gamma_n' \ln R - k'^2)\left(\gamma_n'^2 - 3k'^2 - s'\frac{T}{\tau}\right) + i(\gamma_n'^2 - k'^2)\right] \exp \gamma_n', \tag{25g}$$

$$G_{2n} = \frac{1}{k'}\left[-\frac{1}{\ln R}\frac{is'\gamma_n'}{k'^2}(\gamma_n'^2 - \gamma_n' \ln R - k'^2)\left(\gamma_n'^2 - 3k'^2 - s'\frac{T}{\tau}\right) + i(\gamma_n'^2 - k'^2)\right], \tag{25h}$$

$$G_{3n} = \frac{s'}{k'^2 \ln R}[\gamma_n'^2 + k'^2][\gamma_n'^2 - \gamma_n' \ln R - k'^2] \exp \gamma_n', \tag{25i}$$

$$G_{4n} = \frac{s'}{k'^2 \ln R}[\gamma_n'^2 + k'^2][\gamma_n'^2 - \gamma_n' \ln R - k'^2], \tag{25j}$$

$$G_{5n} = -\gamma_n' \exp \gamma_n', \quad G_{6n} = -R\gamma_n'. \tag{25k, l}$$

Finally, a set of transfer relations may be written down to characterize the layer in terms of perturbation complex amplitudes at its surfaces. Equations (22) and (23) combine to give

$$\mathbf{S} = \mathbf{Q}\mathbf{V}, \quad \mathbf{Q} = \mathbf{G}\mathbf{H}^{-1}. \tag{26), (27}$$

6. Layer spliced to bounding half-spaces

Provided that the region of conductivity variation is thin and perturbation wavelengths are short compared with the thicknesses of the fluid regions bounding the layer of varying conductivity, these can be modelled as half-spaces. Because there is no equilibrium conductivity gradient outside the layer, no perturbation charge is induced by fluid motions in the bounding regions [see (11) and (12)]. Thus the perturbation fluid dynamics of the bounding regions are governed by (14) with $\hat{\rho}_f = 0$. Conditions are imposed as $x \to \pm\infty$, then, by discarding growing solutions. The result is a set of transfer relations for the bounding half-spaces, with a and b referring to boundaries at $x = \Delta$ and $x = 0$ respectively:

$$\begin{bmatrix} \hat{S}_x'^a \\ \hat{S}_z'^a \end{bmatrix} = \mathbf{P}^a \begin{bmatrix} \hat{v}_x'^a \\ \hat{v}_z'^a \end{bmatrix}, \tag{28}$$

$$\hat{J}_x'^a = k'\hat{\phi}'^a, \tag{29}$$

$$\begin{bmatrix} \hat{S}_x'^b \\ \hat{S}_z'^b \end{bmatrix} = \mathbf{P}^b \begin{bmatrix} \hat{v}_x'^b \\ \hat{v}_z'^b \end{bmatrix}, \tag{30}$$

$$\hat{J}_x'^b = -Rk'\hat{\phi}'^b, \tag{31}$$

where

$$\mathbf{P}^a = \begin{bmatrix} -q'k'^{-1}(k'+q') & i(k'-q') \\ i(q'-k') & -(q'+k') \end{bmatrix},$$

$$\mathbf{P}^b = \begin{bmatrix} q'k'^{-1}(k'+q') & i(k'-q') \\ i(q'-k') & q'+k' \end{bmatrix},$$

$$q' \equiv (k'^2 + s'T/\tau)^{\frac{1}{2}} \quad (\mathrm{Re}\, q' > 0)$$

and the relations are written assuming $k' > 0$.

Combination of (26) and (28)–(31) yields

$$\mathbf{F}\mathbf{V} = 0, \tag{32}$$

where V is defined by (24) and

$$\mathbf{F} = \begin{bmatrix} Q_{11} - P_{11}^a & Q_{12} & Q_{13} - P_{12}^a & Q_{14} & Q_{15} & Q_{16} \\ Q_{21} & Q_{22} - P_{11}^b & Q_{23} & Q_{24} - P_{12}^b & Q_{25} & Q_{26} \\ Q_{21} - P_{21}^a & Q_{32} & Q_{33} - P_{22}^a & Q_{34} & Q_{35} & Q_{36} \\ Q_{41} & Q_{42} - P_{21}^b & Q_{43} & Q_{44} - P_{22}^b & Q_{45} & Q_{46} \\ Q_{51} & Q_{52} & Q_{53} & Q_{54} & Q_{55} - k' & Q_{56} \\ Q_{61} & Q_{62} & Q_{63} & Q_{64} & Q_{66} & Q_{66} + Rk' \end{bmatrix}. \tag{33}$$

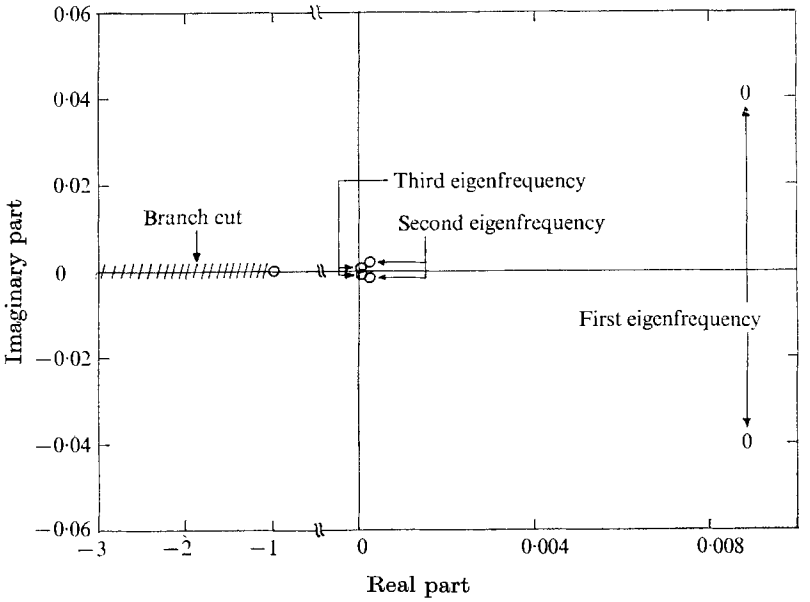

FIGURE 7. Zeros and branch cut of the complex function $D(s')$ for $k' = 1$, $T/\tau = 1$, $R = 2{\cdot}72$. The branch cut characterizes viscous decay in the bounding half-spaces. An infinite set of zeros in the right half-plane corresponds to growing, propagating internal modes.

For non-trivial solutions to (33), the dispersion relation takes the form

$$D \equiv \det \mathbf{F} = 0. \tag{34}$$

For given k', T/τ and R, a search must be carried out in the complex s' plane for values of s' where (34) is satisfied. In a region near a zero of $D(s')$, provided that this function is analytic, the zero may be approached by changing s' by (Betchov & Criminale 1967)

$$\Delta s' = -\lambda \frac{D(s')}{[dD/ds']_{s'}}, \tag{35}$$

where $\lambda \leqslant 1$. To determine $[dD/ds']_{s'}$, a small exploratory step $\delta s'$ some fraction of the previous $\Delta s'$ is taken:

$$\delta s' = \mu \Delta s', \tag{36}$$

where $\mu < 1$. Then

$$[dD/ds']_{s'} \simeq \frac{D(s'+\delta s') - D(s')}{\delta s'}. \tag{37}$$

Normally the parameters are set at $\mu = 0{\cdot}1$ and $\lambda = 1$, but when there is difficulty with convergence λ is reset to $0{\cdot}5$.

The function $D(s')$ has complex-conjugate symmetry about the real s' axis. That is, the value of D at a point $s'_r + is'_i$ is the complex conjugate of the value at the point $s'_r - is'_i$. Thus, only a search for zeros in the upper half-plane need be carried out. Figure 7 shows the singularities of the function D in the complex s' plane. The function has a branch cut, extending leftwards along the s'_r axis

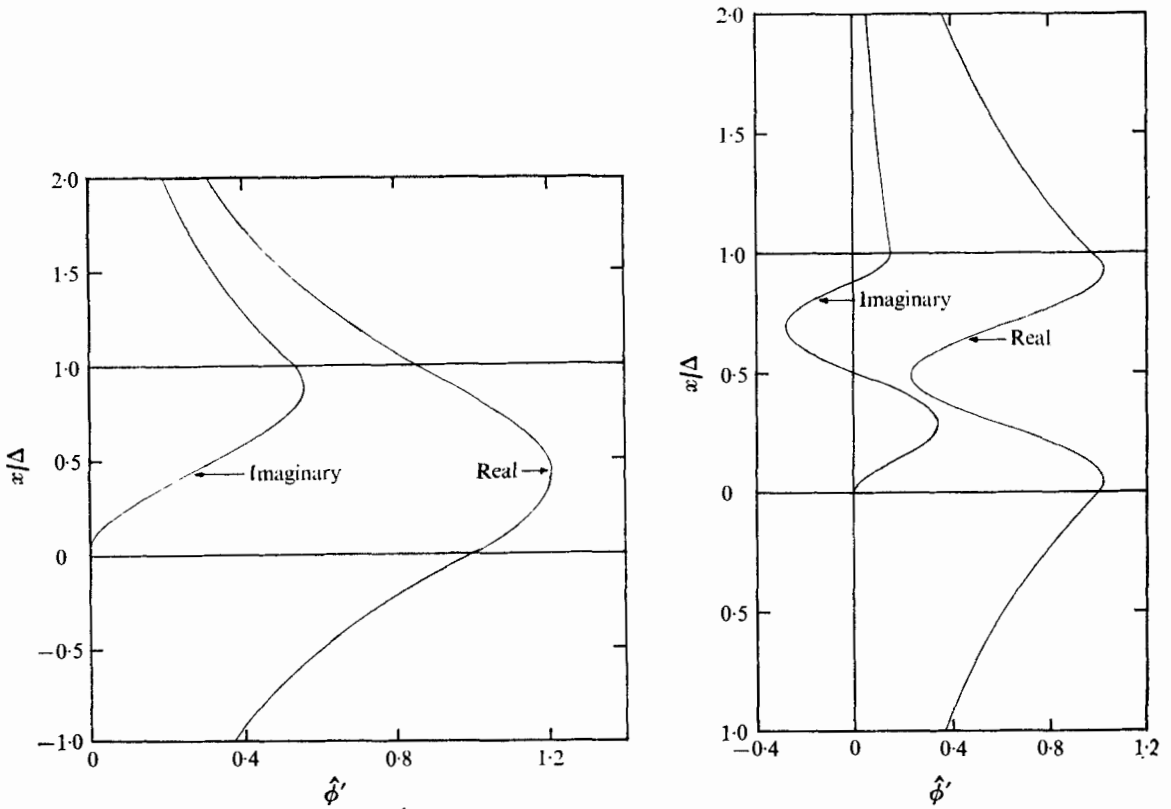

FIGURE 8. Eigenfunctions $\hat{\phi}'(x/\Delta)$ at $k' = 1$, $T/\tau = 1$, $R = 2{\cdot}72$. (*a*) First eigenfunction: $s' = 0{\cdot}00841 + i0{\cdot}0393$. (*b*) Second eigenfunction: $s' = 0{\cdot}000197 + i0{\cdot}00198$. Higher (less rapidly growing) modes involve more and more points of zero slope within the layer.

from a branch point at $s' = -k'^2T/\tau + i0$ to negative infinity. To the left of the branch point, in crossing the negative real axis, when s' is changed incrementally from $s_r + i\delta$ to $s_r - i\delta$, the function D has a discontinuous imaginary part, i.e. it jumps from $D_r + iD_1$ to $D_r - iD_i$, where D_i is non-zero. This non-analyticity traces back to the determination of q', the viscous decay number, as defined with (28).

There is an infinite set of zeros (eigenfrequency solutions to (34)) in the right half-plane with non-zero s_i'. Of all the zeros, the one with the largest s_r' is termed the first eigenfrequency, the one with the second largest s_r' the second eigenfrequency, and so on. The first eigenfrequency is found also to have the largest value of s_i', and so on. As is characteristic of internal mode problems, there is an infinite set of eigenfrequencies in the right upper half-plane, all within a rectangular region with corners at the first eigenfrequency and the origin. Any one eigenfrequency has an infinite set of eigenfrequencies between itself and the origin.

To understand better the significance of the various eigenfrequencies, it is desirable to determine the distributions of the perturbation complex amplitudes of physical quantities as functions of the x co-ordinate (the eigenfunctions). This may be accomplished as follows.

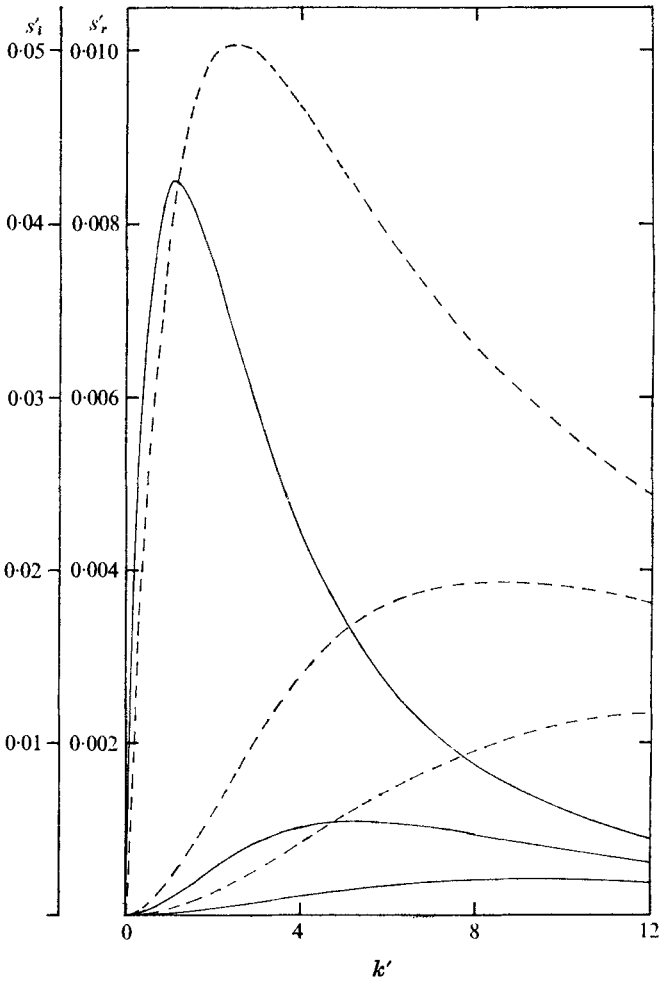

FIGURE 9. $s'_r(k')$ (solid curves) and $s'_i(k')$ (dashed curves) for first three eigenfrequencies at $T/\tau = 1$, $R = 2{\cdot}72$. Each mode has a value of k' where s'_r is a maximum. For the first eigenfrequency, this value is termed k'^*, and $s'_r(k'^*) \equiv s_r^*$ and $s'_i(k'^*) \equiv s_i^*$.

Having found a value of s' where (34) is satisfied, a non-trivial column vector **V** satisfying (32) is determined by taking linear combinations of rows of **F** so as to produce zero entries everywhere below the main diagonal. Having performed such manipulations, because $D = 0$, the 6, 6 element will become zero. Thus the value of $\hat{\phi}'^b$ may be arbitrarily set to

$$\hat{\phi}'^b = 1 + i0. \tag{38}$$

Then, the manipulated set of equations derived from (32) is used to determine the values of all the other variables in **V**. Equation (22) is then inverted to compute the corresponding **A**, i.e. the $\hat{\Phi}'_n$. The various physical quantities, $\hat{\phi}'$, $\hat{v}'_x$, $\hat{v}'_z$, $\hat{J}'_x$, $\hat{S}'_x$ and S'_z, may then be directly computed. Figure 8 (*a*) shows the eigenfunction $\hat{\phi}'$ for the first eigenfrequency at $k' = 1$, $T/\tau = 1$ and $R = e$.

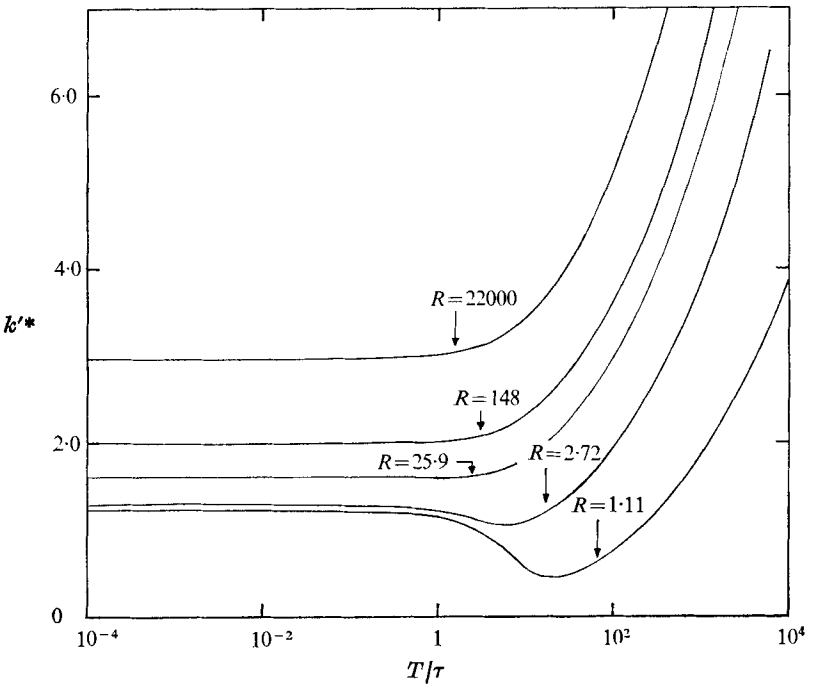

FIGURE 10. k'^* *vs.* T/τ for various values of R. For $T/\tau \ll 1$, k'^* is independent of T/τ and increases with R.

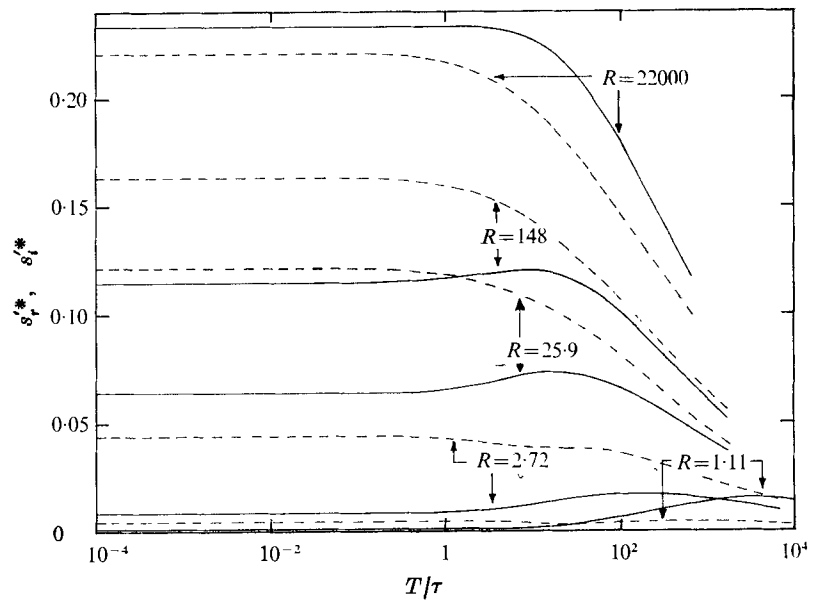

FIGURE 11. $s_r'^*$ (solid curves) and $s_i'^*$ (dashed curves) *vs.* T/τ for various values of R. In the viscous-dominated regime $T/\tau \ll 1$, $s_r'^*$ and $s_i'^*$ are independent of T/τ. Non-zero $s_i'^*$ indicates propagation or overstability.

Real and imaginary parts (showing the distribution at two values of z spaced $\pi/2k$ apart, or at two values of t spaced $\pi/2s_i$ apart) are shown as functions of x/Δ across the varying-conductivity layer and one layer thickness into the half-spaces on either side of the layer. Figure 8 (*b*) shows the eigenfunction $\hat{\phi}'$ for the second eigenfrequency at $k' = 1$, $T/\tau = 1$ and $R = e$. As would be expected, the most rapidly growing mode involves the least variation of physical quantities across the layer. Higher (less rapidly growing) modes involve more and more points of zero slope within the layer.

The dependence of the first three complex eigenfrequencies on k' is described by figure 9. For small k' (waves long compared with the layer thickness), all eigenfrequencies approach zero. In this limit, the situation approaches the surface-coupled model, i.e. an abrupt interface with no first-order electromechanical coupling. At the opposite extreme, for large k', where eigenfunctions vary rapidly across the layer, all eigenfrequencies approach zero asymptotically. At some intermediate k', the real and imaginary parts take on maximum values. For the same mode, the maxima of the real and imaginary parts occur at different values of k'. Maxima occur at increasing values of k' for higher modes.

At $k' = k'^*$, $\mathrm{Re}\, s'$ for the first eigenfrequency has its maximum $\mathrm{Re}\, s'^*$ for any given T/τ and R. Figures 10 and 11 are plots of k'^*, and $s_r'^*$ (solid curves) and $s_i'^*$ (dashed curves), respectively, as functions of T/τ on a logarithmic scale for five values of R. For $T/\tau \ll 1$, viscous effects dominate over inertia, and k'^* and s'^* are independent of T/τ. Thus, if T/τ is varied in this range by varying E_0, holding all other parameters constant, k^* remains constant while s^* increases quadratically with E_0. Alternatively, if T/τ is varied by varying Δ, k^* decreases as $1/\Delta$ while s^* remains constant.

For $T/\tau \gg 1$, inertia plays an important role in the instability dynamics, and k'^* increases while $s_r'^*$ and $s_i'^*$ decrease with increasing T/τ. Note, however, that because T/τ is plotted on a logarithmic scale in figures 7 and 8 the functions are relatively insensitive. Thus, if E_0 is again increased, k^* increases slowly, while s_r^* and s_i^* increase less rapidly than quadratically with E_0. If E_0 is held constant and Δ increased, k^* decreases less rapidly than $1/\Delta$ and s_r^* and s_i^* decrease.

Finally, k^*, s_r^* and s_i^* are relatively insensitive to R, but all three functions increase with R, except in one regime. For large T/τ, s_r^* first decreases, then increases with R.

7. Physical mechanism

The physical nature of the instability described here is made apparent by plotting velocity streamlines, as shown in figure 12. Here $T/\tau = 10^{-4} \ll 1$, so the flow is dominated by viscous effects. Streamlines are plotted across the layer width and one layer thickness into each of the bounding half-spaces. The negative, imaginary part of s'^* indicates propagation of the entire picture to the left. The corresponding eigenfrequency with positive imaginary part would have streamlines slanted to the right, with the entire picture propagating to the right.

The physical mechanism responsible for overstable modes in the configuration

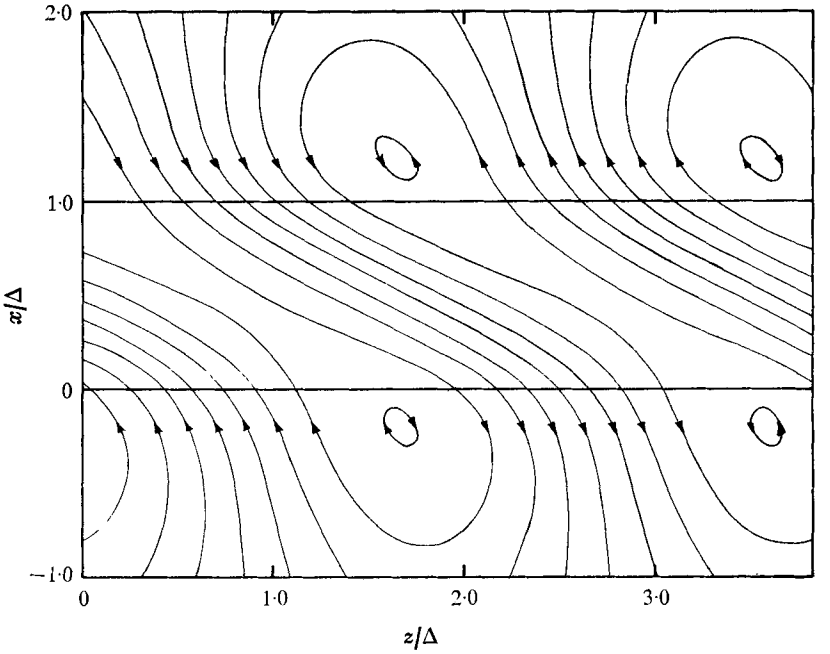

FIGURE 12. Fluid velocity streamlines at $T/\tau = 10^{-4}$, $R = 25{\cdot}9$, $k' = k'^* = 1{\cdot}641$, $s' = s'^* = 0{\cdot}0640 - 0{\cdot}1233i$. With the more conducting fluid below and the direction of streamline slant as shown, the slant vector $\boldsymbol{\kappa}$ points outwards and $\nabla\sigma_0 \times \boldsymbol{\kappa}$ points to the left, the direction of propagation. The mirror-image eigenfrequency, with $s_i'^* > 0$, would have streamlines slanting and propagating in the opposite direction.

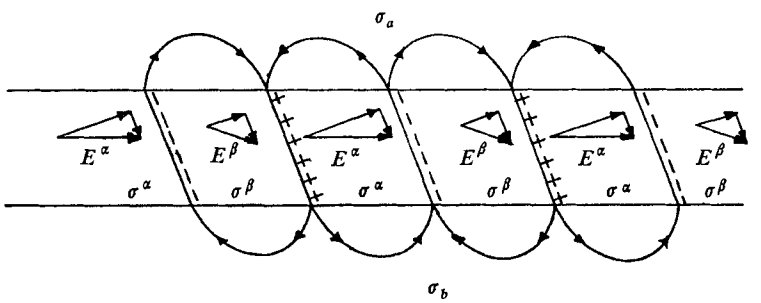

FIGURE 13. Physical mechanism responsible for growth and propagation. Surface charge accumulates at slanted interfaces and causes cellular fluid motions. Consequent conductivity alteration leads to propagation.

described may be understood with the help of figure 13. Within the region of varying conductivity, bounded above and below by half-spaces, slanted layers of alternating low and high conductivities σ^α and σ^β are postulated. (The actual variation, both in the theory described by figure 12 and in the experimental photographs in figure 2, is smooth. The dependence is discretized here as a means of simplifying the mechanism but retaining the essence of the interaction.) Application of an electric field in the horizontal direction in the leftmost layer

leads to surface charge accumulation at the slanted interfaces so as to yield a continuous normal current density. Interfaces bounded on the left by a layer of low conductivity and on the right by a layer of high conductivity experience an upward-directed shear force owing to the tangential electric field component. Similarly, interfaces bounded on the left by a layer of high conductivity and on the right by a layer of low conductivity experience a downward-directed shear force. The resulting cellular fluid motions alter the conductivity distribution by drawing in less conducting fluid from the upper half-space and more conducting fluid from the lower half-space. This effectively propagates the slanted layer structure to the left, as is the case for eigenvalue solutions with $s_i < 0$.

If rightward slanted layers are postulated at the outset, the resulting surface charge accumulation, fluid motions and conductivity alterations lead to a rightward-propagating structure, corresponding to the mirror-image eigenvalue solutions with $s_i > 0$.

Reversal of the direction of the equilibrium electric field does not alter the physical mechanism described here. The propagation direction depends only upon the assumed direction of slant and orientation of high and low conductivity regions. The maximum growth rate as a function of wavenumber is attained by optimizing the cell size (and resulting slant angle) with respect to the competition between electrically driven shearing forces and retarding viscous drag and inertia (if significant).

The direction of propagation of a cell having a given slant is, in general, determined by the following rule: if $\boldsymbol{\kappa}$ is defined as a vector obtained by crossing the direction of slant through an acute angle into the horizontal direction and $\nabla\sigma_0$ is the gradient of the equilibrium conductivity distribution, then the cell propagates in the direction $\nabla\sigma_0 \times \boldsymbol{\kappa}$.

Of course, the exponential conductivity distribution of the viscous layer only approximates the diffusive distribution which actually joins the two regions of uniform conductivity. However a stability analysis of the sort presented is not expected to be sensitive to the details of this distribution. The analysis provides a clear indication that, in situations involving conductivity gradients normal to an applied electric field, internal electrohydrodynamic coupling can result in an instability tending to augment the conductivity diffusion process.

8. Rigid equipotential boundaries

To distinguish further the instability modelled above from a surface-coupled instability, the fluid half-spaces are removed and the varying-conductivity layer is bounded with rigid equipotential (in the perturbation sense) boundaries. In this way, the 'interface' region is isolated and the dynamics are clearly internal to the layer.

The boundary conditions at the layer surfaces then become simply

$$\mathbf{V} = 0. \tag{39}$$

For non-trivial $\mathbf{S}$ the dispersion relation takes the form

$$D' \equiv \det \mathbf{Q}^{-1} = 0. \tag{40}$$

Again, an infinite set of overstable eigenfrequencies is found. The branch cut is replaced by an infinite discrete set of pure real, decaying eigenfrequencies.

The eigenfrequencies as a function of k' and eigenfunctions have forms much like those obtained with a layer bounded by half-spaces.

9. Correspondence between experiment and theory

Comparison of the slanted fronts experimentally observed in figure 2 with the cells in figure 12 requires that the photographs be turned upside down, so that the more conducting fluid is at the bottom. Alternatively, the cross-product defined in §7 may be used to see that the fronts slant and propagate in the manner described by the theory.

It is essential to recognize here that detailed correlation between experiment and theory cannot be claimed for two reasons: first, the experimental configuration is not well enough controlled, on the scale of the processes described; second, the detailed evolution of the instability from initial noise is not simply determined by the fastest growing wavenumber.

There is, however, strong evidence that the experimentally observed fine-scale processes are explained by the physical mechanism identified by the theory. The slant angle of fluid streamlines in the centre of the cells in figure 12 (27°) falls within the experimentally determined range (20°–30°). The wavenumber k associated with the spatial periodicity of the experimental fronts is halved when the interface is allowed to diffuse to double its initial thickness. This corresponds to $k'^* = k^*\Delta =$ one known number, dependent only on R and T/τ in the theory.

Finally, it is possible, by starting with two different bits of experimental data and working back through the theory, to arrive by two different routes at an estimate of the initial interface thickness. Consider the last sequence in figure 2, for example, in which

$$E_0 = 1{\cdot}82 \times 10^4 \text{ V/m}, \quad \tau = \eta/\epsilon E_0^2 = 6{\cdot}63 \text{ s}, \quad R = 25{\cdot}9.$$

Assuming $T/\tau \ll 1$, figures 9 and 10 yield

$$s_r'^* = 0{\cdot}064, \quad s_i'^* = 0{\cdot}123, \quad k'^* = 1{\cdot}641.$$

Measurement of the distance between fronts in figure 2(n) and the assumption that it may be identified with the fastest growing wavenumber yield

$$2\pi\Delta/k^* = 3{\cdot}9 \times 10^{-3} \text{ m},$$

which implies $\Delta = 10^{-3}$ m. Measurement of the velocity of the front from figures 2(m)–(n)–(o) and the assumption that it may be identified with the phase velocity s_i^*/k^* yield

$$s_i'^*\Delta/k'^*\tau = 1{\cdot}2 \times 10^{-5} \text{ m/s},$$

which also implies $\Delta = 10^{-3}$ m. Checking the validity of the assumption $T/\tau \ll 1$ gives

$$T = \rho\Delta^2/\eta = 0{\cdot}0154 \ll \tau.$$

Thus the assumption that experimentally observed fronts correspond to the theoretically predicted propagating cells leads to consistent prediction of the interface thickness from two separate pieces of experimental data.

Propagating fronts in a region of spatially varying fluid conductivity are suggestive of similar phenomena observed in poorly conducting fluids with thermally induced property gradients (Turnbull 1968*b*). Propagation of the phases of unstable modes is, similarly, consistent with a bulk-coupled electrohydrodynamic theory (Turnbull 1968*a*).

10. Conclusions

It is important to realize that the theory of the varying-conductivity layer is associated with a bulk-coupled instability. An abrupt-discontinuity model can never account for this sort of internal instability. In the language of a surface-coupled model, the coupling mechanism is 'within the interface itself'. Nevertheless, the constant-conductivity regions bounding the layer are disturbed by the instability. That is, the eigenfunctions – potential, current, velocity and stress distributions – extend into the bounding regions. Thus the instability provides an electrohydrodynamic mechanism for conductivity, mass and momentum transport across the layer.

The unstable nature of the varying-conductivity layer has been further confirmed by bounding it with rigid equipotential walls.

Experimental studies show evidence of instability on the interfacial scale, apparently a manifestation of the physical mechanism described by the theory. In addition, large-scale violent electrohydrodynamic mixing processes dominate what is seen at relatively high values of the electric field. Even in this case, where the phenomena are highly nonlinear and complex, photocell measurements confirm that distributions of average fluid properties evolve in time on a scale determined by the electric–viscous time $\eta/\epsilon E^2$.

Both theory and experiment point clearly to important electromechanical mechanisms inducing convection in situations involving fluid media with conductivity gradients. A fundamental understanding of such interactions is of practical importance in electrochemical processing, electrophoretic analysis, and electrically driven fluid mixing schemes in general.

This work was supported by NSF Grant GK-40021.

REFERENCES

BETCHOV, R. & CRIMINALE, W. O. 1967 *Stability of Parallel Flows*, p. 78. Academic.

LEVICH, V. G. 1962 *Physicochemical Hydrodynamics*, chap. 2. Prentice-Hall.

MELCHER, J. R. 1972 Electrohydrodynamics. *Applied Mechanics. Proc. 13th Int. Cong. Theor. Appl. Mech., Moscow*, pp. 240–263. Springer.

MELCHER, J. R. & SCHWARTZ, W. J. 1968 Interfacial relaxation overstability in a tangential electric field. *Phys. Fluids*, **11**, 2604–2616.

TURNBULL, R. J. 1968*a* Electroconvective instability with a stabilizing temperature gradient. I. Theory. *Phys. Fluids*, **11**, 2588–2596.

TURNBULL, R. J. 1968*b* Electroconvective instability with a stabilizing temperature gradient. II. Experimental results. *Phys. Fluids*, **11**, 2597–2603.

UHL, V. W. & GRAY, J. B. 1966 *Mixing Theory and Practice*, vol. I, chap. 1. Academic,

WOODSON, H. H. & MELCHER, J. R. 1968 *Electromechanical Dynamics*. Part II. *Fields, Forces, and Motion*, p. 383. Wiley.

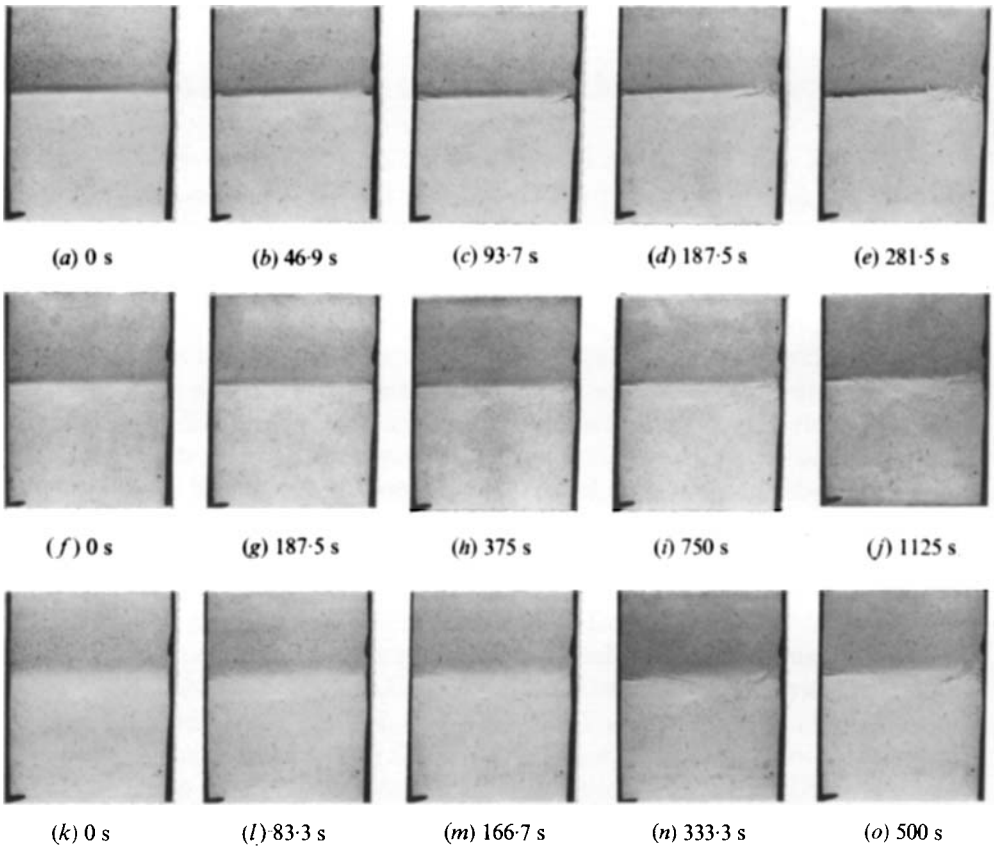

FIGURE 2. Photographs of fluid-component distributions in experimental cell. Time intervals are scaled to $1/E^2$. The upper fluid is more conducting. Sequence (*a*)–(*e*): $E = 2{\cdot}42 \times 10^4$ V/m; interface diffused 1 h. Sequence (*f*)–(*j*): $E = 1{\cdot}21 \times 10^4$ V/m; interface diffused 1 h. Sequence (*k*)–(*o*): $E = 1{\cdot}82 \times 10^4$ V/m; interface diffused 4 h.

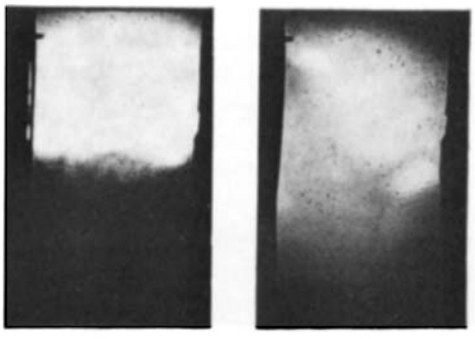

FIGURE 3. Photographs of fluid-component distributions in experimental cell at relatively high electric fields. The lower fluid is more conducting. (*a*) $E = 6{\cdot}06 \times 10^4$ V/m; $t = 60$ s. (*b*) $E = 6{\cdot}06 \times 10^5$ V/m; $t = 60$ s.